Residual axial compression capacity of localized blast-damaged RC columns

Ke-Chiang Wu [a,b], Bing Li [a,], Keh-Chyuan Tsai [b]*

[a] School of Civil and Environmental Engineering, Nanyang Technological University, Singapore 639798, Singapore

[b] Department of Civil Engineering, National Taiwan University, Taipei 10617, Taiwan

[*] Corresponding author. Tel.: +65 67905090. E-mail address: cbli@ntu.edu.sg (B. Li).

Abstract

The risks associated with suitcase bombs are of serious concern because they can be easily handled and placed within close proximity of key structural components of building structures. The most common failure mode of the structures subjected to blast loads from satchel and suitcase bombs is progressive collapse. High-fidelity physics based computer program, LS-DYNA is utilized in this study to provide numerical simulations of the dynamic response and residual axial capacity of reinforced concrete (RC) columns subjected to blast loads. Field tests using near-field explosive charge were conducted on two RC column specimens. The test results were compared with the analytical results to validate the finite element model. An extensive parametric study was conducted to investigate the relationship between residual axial capacity and structural and loading parameters such as material strength, column detail and blast conditions. Two empirical equations were derived through a multivariable regression analysis in terms of the various parameters to predict the residual capacity index based on a non-dimensional column dimension parameter (ωTNT). According to the proposed equations, the residual capacity index can be determined and compared with a service axial load index

Keywords: LS-DYNA; Near-field explosive test; RC column; Residual axial capacity

1. Introduction

Blast loads and its effects on structures have received considerable attention in recent years due to the many accidental or intentional events that have damaged important structures. The most common failure mode caused by blast loadings is progressive collapse. One of the most useful information when assessing the possibility of progressive collapse of a blast-damaged structure would be the residual axial capacity of its columns. There are two main analytical methods for blast-resistant design. The first method utilizes structural dynamic analysis to determine the maximum responses for structure under blast loads [1, 2]. The second method utilizes an explosive test or finite element analysis to determine the column behavior when subjected to blast loads [3, 4]. As the explosive test is a very costly option, finite element analysis was utilized to carry out the blast-resistant design in this study.

When the structures are subjected to blast loads, its structural components may respond at very high strain rate of up to an order of 10-1000 s^{-1} or even higher. At such high strain rates, the apparent strength of the materials can significantly increase, by more than 50% for the steel, 100% for concrete in compression, and in excess of 600% for concrete in tension [5]. In this research, two RC and one SRC column specimens were utilized and subjected to actual contact (for SRC specimen) or with a stand-off (for RC specimens) explosives in a field test [6]. A high-fidelity physics based computer program, LS-DYNA [7] is used to provide numerical simulations of the dynamic response and residual axial capacity of columns subjected to blast loads. In this paper, the test results of the two RC columns are presented and the accuracy of the analytical model is checked by comparing the analytical results with the experimental ones. Parameters with the model such as material strength, column details and blast condition can be changed and its effects on the residual axial capacity of the columns can be studied. Studying several models with different parameters can be helpful to develop an empirical equation capable of predicting the residual axial capacity of blast-damaged columns. An example of such an equation is:

Residual axial capacity = *f* (material strength, column details, blast condition) (1)

2. LS-DYNA analysis of column damages under the blast loads

2.1. Structural geometry

The column considered herein is shown in Fig. 1. Solid elements with a single integration point were used to model concrete while beam elements were used to model steel reinforcing bars. A mesh size of 50 mm is used to create the model. In order to provide higher fidelity for the column constrains, a footing and a head are included in the numerical model, as shown in Fig. 1. The outer vertical face of footing and head were constrained against horizontal motions (i.e., in the x- and y-direction) and the bottom face of footing is constrained against vertical motion (i.e., in the z-direction). In the numerical simulations, a perfect bond is assumed between the concrete and the steel. The steel reinforcing bars were modeled explicitly using beam element. As a result, "shared nodes" are used between the concrete mesh and the steel reinforcement mesh. It is assumed that perfect bond exists and there is no slip occurs at these shared nodes.

2.2. Material model

2.2.1. Concrete

The Finite element code LS-DYNA, which is used in this research, contains several material models that can be used to represent concrete, namely, material type 5 (Soil and Crushable Foam), material type 14 (Soil and Crushable Foam Failure), material type 16 (pseudo tensor), material type 25 (geological cap model), material type 72RW3 (concrete damage), material type 84(winfrith concrete), and material type 96 (brittle damage). Material type 72 RW3 (MAT_CONCRETE_DAMAGE_REL3), was the third release of Karagozian and Case (K&C) concrete model. It is a plasticity-based model, using three shear failure surfaces and including damage and strain-rate effects [8]. The model has a default parameter generation function based on the unconfined compressive strength of the concrete. In this model, the stress tensor is expressed as the sum of the hydrostatic stress tensor and the deviatoric stress tensor. The

hydrostatic tensor changes the concrete volume and the deviatoric stress tensor controls the shape deformation.

A three-curve model is used to analyze the deviatoric stress tensor, as shown in Fig. 2, where the upper curve represents the maximum strength curve, the middle curve is the initial yield strength curve and the lower curve is the failed material residual strength curve.

Concrete has a complex non-linear compression behavior because of its large-scale heterogeneity and a porosity of typically 10%. The compaction model for concrete used here is defined as follows:

$$p = C(\varepsilon_v) + \gamma T(\varepsilon_v) E \qquad (2)$$

where E is the initial energy per initial volume, γ is the ratio of specific heats. Pressure is determined by the volumetric strain ($\varepsilon_v = (\rho_0/\rho) - 1$) and specific internal energy e where ρ is density and ρ_0 is the reference initial density of solid material as shown in Fig. 3. Comparison between the present compaction model and experimental results in literature [9] for normal concrete of 50 MPaare shown in Fig. 4.

The effect of strain rate is typically represented by a parameter, namely the dynamic increase factor (DIF). It is the ratio of dynamic-to-static strength versus strain rate. Usually, the strain rate effect is also response time history dependent. However, in practice it is always assumed to depend on the strain rate only. The DIF of compressive strength given by CEB [10] is expressed as follows:

$$\text{CDIF} = \frac{f'_{cd}}{f'_{cs}} = \begin{cases} \left(\frac{\dot{\varepsilon}_d}{\dot{\varepsilon}_s}\right)^{1.026\alpha} & , \quad \dot{\varepsilon}_d \le 30\ \text{s}^{-1} \\ \gamma(\dot{\varepsilon}_d)^{\frac{1}{3}} & , \quad \dot{\varepsilon}_d > 30\ \text{s}^{-1} \end{cases} \qquad (3)$$

where f'_{cd} is the dynamic compressive strength at the strain rate $\dot{\varepsilon}_d$, $\dot{\varepsilon}_s = 30 \times 10^{-6} s^{-1}$, $\log\gamma = 6.15\alpha - 0.492$, $\alpha = (5 + 3f_{cu}/4)^{-1}$, f'_{cs} is the static compressive strength and f_{cu} is the static cube compressive strength in MPa. Fig. 5 shows the comparison between the experimental results and the CEB empirical results. CEB also recommends the use of the DIF to determine the tensile strength of concrete. However, it was noted during comparing available experimental results with the CEB empirical results, that the tensile DIF recommended by CEB was substantially underestimated as illustrated in Fig. 6. For this reason, the modified CEB formulation [11] is used to estimate the DIF of tensile strength as follows:

$$\text{TDIF} = \frac{f_{td}}{f_{ts}} = \begin{cases} \left(\frac{\dot{\varepsilon}_d}{\dot{\varepsilon}_s}\right)^{\delta} & , \quad \dot{\varepsilon}_d \le 1\ \text{s}^{-1} \\ \beta\left(\frac{\dot{\varepsilon}_d}{\dot{\varepsilon}_s}\right)^{\frac{1}{3}} & , \quad \dot{\varepsilon}_d > 1\ \text{s}^{-1} \end{cases} \qquad (4)$$

where f_{td} is the dynamic tensile strength at the strain rate $\dot{\varepsilon}_d$ $\dot{\varepsilon}_s = 10^{-6} s^{-1}$, $\log\beta = 6\delta - 2$, $\delta = (1 + 8f'_c/f'_{co})^{-1}$, f'_c is the static compressive strength in MPa and f'_{co}=10 MPa. The strain rate effects on Eq. (3) and Eq. (4) are only in the strain rate range of 10^6-1000 s^{-1}. When the strain rate is higher than 1000 s^{-1}, DIFs for 1000 $s^{-1}$are used to avoid overestimation of the strain rate effect. Once the DIFs are calculated, a dynamic compressive strength and a dynamic tensile strength are obtained by multiplying the DIF with the respective static strength.

The element erosion function, while not a material property or physics based phenomena provides a useful means to simulate the spall of concrete and produce response plots that provide a more realistic graphical representation of the actual blast events. The erosion feature is characterized by a physical separation of the eroded solid element from the rest of the mesh. In this study, elements are eroded when their principle tensile strains reach 10 percent.

2.2.2. Steel

The steel within the column is modeled as a strain sensitive uniaxial elastic-plastic material to account for its strain rate sensitivity as well as stress-strain history dependence. Material model PIECEWISE_LINEAR_PLASTICITY (MAT_024) from LS-DYNA is utilized in this study to incorporate the strain rate effect. The expressions proposed by Malvar [5] on strain rate effect are utilized in this study. Fig. 7 shows this proposed DIF for both yield and ultimate stress. The DIF for steel can be expressed as follows:

$$\text{DIF} = \left(\frac{\dot{\varepsilon}}{10^{-4}}\right)^{\alpha} \tag{5}$$

where for the yield stress, $\alpha = \alpha_{fy}$ is expressed as follows:

$$\alpha_{fy} = 0.074 - 0.040\,\frac{f_y}{414} \tag{6}$$

and for the ultimate stress, $\alpha = \alpha_{fu}$ is expressed as follows:

$$\alpha_{fu} = 0.019 - 0.009\,\frac{f_y}{414} \tag{7}$$

and where the strain rate equation is in s^{-1} and f_y is the yield strength in MPa. Eq. (5) is valid with yield stresses between 290 and 710 MPa, and for strain rates between 10^{-4} and 10 s^{-1}.

2.3. Simulation of blast loads used in hydrocodes

The Arbitrary LagrangeeEuler (ALE) approach was used to model the interface between the air and the structure. LS-DYNA applies a coupled methodology to allow an optimum numerical solution. Using this approach, different domains of a physical problem such as structures and fluids can be modeled simultaneously using different numerical techniques. These different domains are then coupled together in space and time. These features make this computer program especially suitable for the study of interaction problems involving multiple systems of structures and fluids.

In the numerical model, air is assumed to be an ideal gas that is able to satisfy the equation of state (EOS). The pressure related to the energy can be expressed as follows:

$$p = (\gamma - 1)\rho e \tag{8}$$

where γ is a constant, ρ is the air density and e is the specific internal energy. In this study, the parameters in Eq. (8) given in Table 1.

High explosives (TNT) are typically modeled by using the Jonese-Wilkinse-Lee (JWL) EOS, which models the pressure generated from the chemical energy in an explosion. It can be expressed as follows:

$$p = A\left(1 - \frac{\omega}{R_1 v}\right)e^{-R_1 v} + B\left(1 - \frac{\omega}{R_2 v}\right)e^{-R_2 v} + \frac{\omega e}{v} \tag{9}$$

where p is the hydrostatic pressure, ν is the specific volume, e is the specific internal energy, and A, B, R_1, R_2, and ω are the material parameters. In this study, the parameters in Eq. (9) are given in Table 2.

The geometry of the explosive charge used in the numerical simulation was identical to that used in the experimental work. During the numerical computation, the geometrical extent of the air was kept unchanged. However, the air is responsible to propagate the blast wave.

2.4. Analytical procedure

The following analytical procedures are applied to the parametric study presented in Section 4.

2.5. Stage 1: (initial stage)

In the initial stage, a linearly increasing axial force up to the service axial load (P_L) is imposed on the column prior to the blast loads to simulate the gravity load effects presented in the column. The time duration for increasing the loads from zero to full service load is 50 ms. This axial force must be applied gradually in an explicit dynamic analysis. The initial axial load applied to the column is dependent on the axial load ratio (ALR) which is expressed as follows:

$$ALR = \frac{P_L}{f'_c A_g} \tag{10}$$

Where f'_c is the compressive strength of concrete and A_g is the gross area of column cross section. The ALR range applied to the analytical columns is from 0.2 to 0.4. This represents a typical ground floor column in a low-to-medium-rise building.

2.6. Stage 2: (blast stage)

Blast loads are applied over the front face of the column. The dynamic analysis for computing the response of the column under blast load needs to be executed for a sufficiently longer time to capture the complete blast response. Since it is extremely time consuming to carry out the simulation until the column reaches the complete response, the simulation is stopped when the velocities at all the nodes are sufficiently small, i.e., less than 0.1 m/s.

2.7. Stage 3: (post-blast stage)

In the post-blast stage, the axial load is gradually increased by applying a downward vertical displacement at the top of the column. Using the method of displacement history, both the residual capacity index and the softening portion of the loading curve can be captured. One typical curve is shown in Fig. 8. It should be noted that in the blast stage, due to the inertia effect, the axial load supported by the column is not constant and it fluctuates with the deformation of the column.

2.8. Stage 4: (vulnerability assessment)

To assess the blast vulnerability of a column, service axial load index (ALI) and residual capacity index (RCI) are defined as follows:

$$\text{ALI} = \frac{P_L}{P_N} \quad \text{and} \quad \text{RCI} = \frac{P_r}{P_N} \tag{11}$$

where P_r is the residual axial capacity of the blast-damaged column and P_N is the nominal strength of the RC column. A column whose ALI is greater than its RCI is considered as failed or collapsed, otherwise, the column is supposed to have sufficient strength for the blast loads.

3. Validation of analytical results

Two RC columns were subjected to a charge, equivalent to 25 kg of TNT that was placed at two different stand-off distances, 200 and 500 mm.

3.1. Experiment specimens

The column specimens were included with a top head and a foundation. Fig. 9 shows the geometry and section details of the test specimens. The RC column specimens were designed based on the specifications provided by standard design codes and geometrically scaled down by two-thirds of the size of the column in a typical twenty-story residential building in Singapore. All the column specimens have a cross-sectional dimension of 400 x 400 mm and a vertical height of 2400 mm. The two RC column specimens were identical. The column specimen had a longitudinal reinforcement of eight T20 bars and transverse reinforcement of shear links formed by R6 bars placed 125 mm apart. The provided longitudinal reinforcement ratio is 1.57% and volumetric ratio of transverse reinforcement is 0.21%.

Ready-mix concrete, with a characteristic compressive strength of 30 MPa at 28 days, 13 mm aggregate size and a slump of 125 mm was used to cast the specimens. Twenty-four 150 x 300 mm test cylinders were also cast and cured under the same conditions to ensure that they are representative of their respective column specimens. The averaged cylinder compressive strength is 40 MPa. This strength value was adopted in the finite element models for response simulation of test specimens.

Two types of steel reinforcement bars, high tensile strength steel bars with a nominal yield strength of 420 MPa and mild steel bars with a nominal yield strength of 280 MPa were used in both the specimens. T20 high tensile strength steel bars were used as longitudinal reinforcement and R6 mild steel bars were used as transverse reinforcement.

3.2. Test setup

The test was conducted by placing a charge, equivalent to 25 kg of TNT above the column specimens. The specimens were all placed horizontally as the TNT charge could be conveniently installed. In this manner, the ground was utilized to act as the lateral support from the floor slab and foundation at the top and bottom ends of the column. The TNT was placed on both specimens at a distance of 900 mm measured along the column axial direction from its foundation. The two RC column specimens had their TNT charge placed at stand-off distances of 200 mm and 500 mm from the face of the column respectively. Fig. 10 illustrates the various configurations at which the TNT charge was placed on the two specimens. Table 3 summarizes the explosive masses and stand-off distances of these specimens. No column axial load was applied in the test.

3.3. Comparisons between analytical and test results

In a contact, or near-field blast loading scenario, extremely high peak overpressure are generated. The equipment utilized to measure the response history of the specimen fails when it is subjected to such high pressure. Thus the test results obtained from the experiments only provide damage profiles such as erosion zone of concrete and deformed shapes of the specimens. The boundary conditions for the test specimens and the analytical models are shown in Figs. 11 and 12. The stand-off distance was created by the polystyrene material. It is assumed that this type of packing material has no significant resistance to the blast loads. Thus, the packing material was modeled as air in the numerical simulation.

Fig. 11(a) shows a photograph of RC column specimen 1 after being subjected to the explosive test. The concrete around the regions of the explosive charge was completely damaged. All the longitudinal reinforcement bars suffered large lateral deformation. The transverse reinforcement bars had also shifted from their initial locations. The core of RC column specimen 1 sustained

serious damage, and can be considered to be fully damaged without any residual axial capacity. The analytical results for RC column specimen 1 are shown in Fig. 11(b). Colors on the fringe plot indicate the amount of maximum principle strain. It is evident that the concrete erosion zone is 1200 mm in length. The analytical crack profile is very similar to the cracks sustained by the specimen from the actual charge, indicating that the numerical simulation produced fairly accurate results. In the separate explosive test of the SRC specimen [6], it was confirmed by the numerical analysis that after the discharge of the explosive, the deformed shape and the deflection of the wide flange steel section encased in the column can be rather accurately predicted. This observation seems to suggest that the physics based numerical model can be a very powerful and reliable tool for parametric study of RC or SRC columns subjected to the effects of contact or near-field explosives [6].

Fig. 12(a) shows a photograph of RC column specimen 2 after being subjected to the explosive test. The damaged profile of this specimen is similar to that of RC column specimen 1, i.e., fully damaged without any residual axial capacity. The analytical results for RC column specimen 2 are shown in Fig. 12(b). It is evident that the concrete erosion zone is 800 mm in length. The analytical crack profile is very similar to the cracks sustained by the specimen from the actual charge, indicating that the numerical simulation produced fairly accurate results.

4. Numerical simulation study

4.1. Numerical simulation matrix

Numerical simulations were performed to evaluate the dynamic response and to estimate the residual capacity index of the blast-damaged RC columns using the analytical models that were initially developed. This was followed by an extensive parametric study on the RC columns. The parameters under consideration include, longitudinal reinforcement ratio ρ_g = 1.5% and 2.5%, transverse reinforcement ratio ρ_v = 1.00% and 0.50%, square column depth h = 0.4 m, 0.6 m and 0.9 m, square column height H = 3 m and 4.4 m and axial load ratio P_L/f'_cA_g = 0.2 and 0.4. The parametric study was carried out on a series of ten RC columns, as illustrated in Fig. 13. All the RC columns were seismically detailed. The spacing of the transverse reinforcement was determined in accordance with the ACI 318 code. Table 4 summarizes the specimen characteristics of the numerical simulation matrix. All of the ten RC column specimens were modeled with the same materials. High tensile strength steel bars with a nominal yield strength of 420 MPa were used as longitudinal reinforcement and mild steel bars with a nominal yield strength of 280 MPa were used as transverse reinforcement. The compressive strength of the concrete was 40 MPa.

4.2. Numerical results of residual capacity index of the blast-damaged RC columns

Dynamic analyses were performed on the entire series of RC columns with various combinations of blast conditions and service axial loads. TNT explosive was used and located at either the bottom of columns or at a height of 1.5 m from the footing of columns. The explosive mass ranges from 2.5 to 25 kg for all specimens except for Specimen RC9. The explosive mass for Specimen RC9 ranges from 20 to 60 kg.

4.2.1. Effect of column depth

A column with a greater depth is generally able to resist a larger impulsive load created from a relatively bigger amount of explosive mass. Increasing the column depth means more concrete area and larger cross section modulus, which will result in an increase in both shear and bending strength of the column. Fig. 14 shows the effect of column depth on the residual capacity index with various TNT explosive masses. In order to combine the effects of the mass of TNT explosive and the depth of column, a non-dimensional column dimension parameter (ωTNT) is proposed, which is defined as the ratio of TNT explosive mass to the mass of a 1 m high concrete column. Fig. 15 shows that the proposed non-dimensional column dimension parameter can not only has the capability to combine the two parameters discussed above but also shows the same trend with the varying column depths.

4.2.2. Effect of column height

The column damage mechanism concerning this contact blast case scenario is seen from the field tests conducted to be local and cross section erosion. The column height does not have any effect on the residual capacity index of the blast-damaged column. Instead it is controlled by the residual cross section area of the columns as shown in Fig. 16.

4.2.3. Effect of explosive location

Fig. 17 shows the typical results of blast-damaged columns with similar TNT masses placed at varying locations. It can be seen that the damage is concentrated at the region where the charge was placed. The concrete at the damage zone has larger strain than other zones and caused it to spall. In addition, when the blast loading is concentrated at the 1.5 m height of column, this region is more flexible than the region near the column ends. Thus, under the effects of same amount of explosive, the strain is larger when the explosive is near the column bottom than that when it is at the 1.5 m column height. When the explosive is located near the column bottom, the rear face spalling is due to the shear rather than the direct shock-induced loading. Therefore, the concrete strain at the damage zone of the explosive at the 1.5 m column height scenario is smaller, which results in less concrete spalling and more of the cross section remaining as compared with the explosive near the column bottom scenario. Fig. 18 shows the effect of explosive location on the residual capacity index of blast-damaged columns. The dotted lines denote analytical results, while the solid lines represent the fitted trend lines.

4.2.4. Effect of axial load ratio

Axially applied service loads were applied onto the column prior to the occurrence of the blast incident. These service loads will influence the behavior of the column under blast condition. In this study, the axial load ratio is varied from 0.2 to 0.4. According to the P-M interaction curve of an RC column, additional axial load will influence the moment capacity of the member. Moreover, the shear strength of an RC column can be increased by increasing its axial load. These phenomena are reflected clearly in the residual capacity index of the blast-damaged columns, as shown in Fig. 19.

4.2.5. Effect of transverse reinforcement ratio

The desired ductile flexural behavior can only be developed when shear capacity exceeds flexural capacity. The ductility of a column depends on the amount and distribution of transverse reinforcement within the plastic hinge region. The shear strength of a column can be increased by increasing its transverse reinforcement ratio. An increase in transverse reinforcement ratio of

a column was also improved its bending capacity by providing additional confinement to the core concrete and supplementary lateral restraint against buckling of the longitudinal reinforcement.

The restraint provided from transverse reinforcement within RC columns is vital where cracks have formed and most of the tensile and flexural capacity has been lost but still requiring the member to resist the compressive force before ductile tension failure of the longitudinal reinforcement occurs. Therefore, the transverse reinforcement is expected to have a significant influence on the failure mode and its respective blast resistance of columns subjected to blast loads. Fig. 20 shows the effect of transverse reinforcement ratio on the residual capacity index of the blast-damaged columns. The results show that the residual capacity index of blast-damaged column with low transverse reinforcement ratio is significantly less than that of a column with high transverse reinforcement ratio.

4.2.6. Effect of longitudinal reinforcement ratio

It is usually assumed that the longitudinal reinforcement would be able to support a portion, limited by its buckling or plastic capacity, of the axial load. In most cases the column collapse is related to the increase of axial load carried by the longitudinal reinforcing bars up till the complete deterioration of its compressive strength carrying capacity. An increase in longitudinal reinforcement ratio provides additional axial load carrying capacity to the column and only limited contribution to its shear strength. Fig. 21 shows the effect of longitudinal reinforcement ratio on the residual capacity index of the blast-damaged columns. The results indicate that increasing longitudinal reinforcement ratio does not affect the blast-damaged level of the column and only provides limited contribution to improve its residual axial capacity.

4.2.7. Empirical equations for determining the residual capacity index of blast-damage RC columns

The parametric study revealed the significance of parameters that affect the residual axial capacity of the blast-damaged RC column. Two empirical equations based on the non-dimensional column dimension parameter were derived through multivariable regression analysis in terms of various parameters to predict the residual capacity index. The empirical equation for the case scenario where the TNT explosive is located at the bottom of column is expressed as follows:

$$\frac{P_r}{P_N} = \left(0.05\rho_g + 0.02\rho_v - 0.00035\right)\omega_{\mathrm{TNT}}^{\left(15\rho_g - 10\rho_v - 0.5\frac{P_L}{f_c' A_g} - 1.725\right)} \leq 1.0 \tag{12}$$

The other empirical equation for the case scenario where the TNT explosive is located at a height of 1.5 m from the footing of column is expressed as follows:

$$\frac{P_r}{P_N} = 1.1 - \left(-300\rho_g - 360\rho_v - 5\frac{P_L}{f_c' A_g} + 20.7\right)\omega_{\mathrm{TNT}} \leq 1.0 \tag{13}$$

The ωTNT of Eq. (12) and Eq. (13) is less than 0.04. A few examples presenting the comparison of the empirical equations with the analytical results are shown in Fig. 22. The dotted lines denote the analytical results, and the solid lines represent the empirical equations. It is observed that for most of the cases, the empirical equations provided an almost similar prediction as the analytical results.

5. Conclusions

The following conclusions were drawn based on the results from the numerical simulation study:

- An increase in column depth results in more concrete area and a larger cross section modulus, which in turn improves both shear and bending strength of the column. As such, a column with a larger depth will suffer milder damage from blast loads and be able to sustain higher axial loads in its post-blast state.
- The analytical results show that the column height does not affect the blast response of columns.
- The service axial load applied on to the column prior to it being damaged by the blast loads. It would affect the behavior of the column when subjected to blast pressures. A column with higher axial load ratio can increase its shear strength so that the damage due to blast load is milder. Therefore, a column with higher axial load ratio can retain more residual axial capacity.
- Increasing the transverse reinforcement ratio will greatly increase the shear capacity of the RC column. It will also improve the bending capacity of the column because it provides confinement to the core concrete and lateral restraint against buckling of the longitudinal reinforcement. The analytical results show that the residual capacity index of blast-damaged RC column with low transverse reinforcement ratio is significantly less than that of the blast-damaged RC column with high transverse reinforcement ratio.
- An increase of the longitudinal reinforcement ratio can cause significant increase in the bending strength of the RC column, but however only makes a little contribution to its shear strength. The analytical results indicate that increasing longitudinal reinforcement ratio has limited contribution to improve residual axial capacity.
- The damage zone of the explosive is located at a height of 1.5 m from the footing of column which is more flexible than the case when the explosive is located at the bottom of column. Therefore, the first case shows milder damage and allows the column to retain more residual axial capacity.
- Two empirical equations were derived by fitting the analytical results in terms of various parameters to predict the residual capacity index based on a non-dimensional column dimension parameter. The comparisons of the empirical equations with analytical results and the distribution of error index show that the empirical equations are able to represent the tendency of variation of the parameters. Given that the equation was formulated based on only two experiments and would require a further range of tests to fully validate the procedure. However, it can be used to provide validations of a qualitative nature.

Acknowledgements

This research was supported by a research grant provided by the Defense Science & Technology Agency (DSTA), Singapore, under the Protective Technology Research Center, Nanyang Technological University, Singapore. Any opinions, findings and conclusions

References

[1] Li B, Rong HC, Pan TC. Drift-controlled design of reinforced concrete frame structures under distant blast conditions-part i: theoretical basis. International Journal of Impact Engineering March 2007; Vol. 34:743-54.

[2] Rong HC, Li B. Deformation- controlled design of RC flexural members subjected to blast loadings. ASCE Journal of Structural Engineering 2008; 134 (No. 10):1598-610.

[3] Thilakarathna HMI, Thambiratnam, DP, Dhanasekar S, Perera NJ. Behaviour of axially loaded concrete columns subjected to transverse impact loads. In: Our World in Concrete and Structures : Green Concrete, 16-18 August 2009, Orchard Plaza, Singapore.

[4] Li B, Huang ZW, Lim CL. The verification of non-dimensional energy spectrum based blast design for reinforced concrete members through actual blast tests. ASCE Journal of Structural Engineering June 2010; 136(No. 6):628-36.

[5] Malvar LJ. Review of static and dynamic properties of steel reinforcing bars. ACI Materials Journal 1998; 95(No. 5):609-16.

[6] Wu KC, "Assessment of reinforced concrete and composite steel-concrete columns to resist the effects of suitcase bombs," Master of Engineering Thesis, Nanyang Technological University, Singapore. 2009. p. 180.

[7] LS-DYNA. Keyword user's manual. U.S.A: Livermore Software Technology Corporation; 2007. Version 971.

[8] Malvar LJ, Crawford JE, Wesevich JW, Simons D. A plasticity concrete material model for DYNA3D. International Journal of Impact Engineering June 1997; 19:847-73.

[9] Gebbeken N, Greulich S, Pietzsch A. Hugoniot properties for concrete determined by full-scale detonation experiments and flyer-plate-impact tests. International Journal of Impact Engineering Nov 2006; 32: 2017-31.

[10] Bischoff PH, Perry SH. Compressive behavior of concrete at high strain rates. Materials and Structures May 1991; 24: 425-50.

[11] Malvar LJ, Rose CA. Review of strain rate effects for concrete in tension. ACI Materials Journal Nov 1998; 95(No. 6):735-9.

List of Tables

List of Figures

γ	1.4
ρ	1.225 kg/m^3
e	206800 J/kg

Table 1

A	373.77 GPa
B	3.7471 GPa
R_1	4.15
R_2	0.9
ω	0.35
e	4905 kJ/kg

Table 2

Specimen	TNT mass (kg)	Stand-off distance (mm)
RC column specimen 1	25	200
RC column specimen 2	25	500

Table 3

Specimen	Cross Section (m)	Column Height (m)	Longitudinal Reinforcement	Transverse Reinforcement
RC61	0.6×0.6	3	20T25 ($\rho_g = 2.5\%$)	T13–100 mm ($\rho_v = 1.0\%$)
RC62	0.6×0.6	3	20T25 ($\rho_g = 2.5\%$)	T13–200 mm ($\rho_v = 0.5\%$)
RC63	0.6×0.6	3	20T19 ($\rho_g = 1.5\%$)	T13–100 mm ($\rho_v = 1.0\%$)
RC64	0.6×0.6	3	20T19 ($\rho_g = 1.5\%$)	T13–200 mm ($\rho_v = 0.5\%$)
RC41	0.4×0.4	3	8T25 ($\rho_g = 2.5\%$)	T13–100 mm ($\rho_v = 1.0\%$)
RC42	0.4×0.4	3	8T25 ($\rho_g = 2.5\%$)	T13–200 mm ($\rho_v = 0.5\%$)
RC43	0.4×0.4	3	8T19 ($\rho_g = 1.5\%$)	T13–100 mm ($\rho_v = 1.0\%$)
RC44	0.4×0.4	3	8T19 ($\rho_g = 1.5\%$)	T13–200 mm ($\rho_v = 0.5\%$)
RC621	0.6×0.6	4.4	20T25 ($\rho_g = 2.5\%$)	T13–200 mm ($\rho_v = 0.5\%$)
RC9	0.9×0.9	3	32T29 ($\rho_g = 2.5\%$)	T13–100 mm ($\rho_v = 1.0\%$)

Table 4

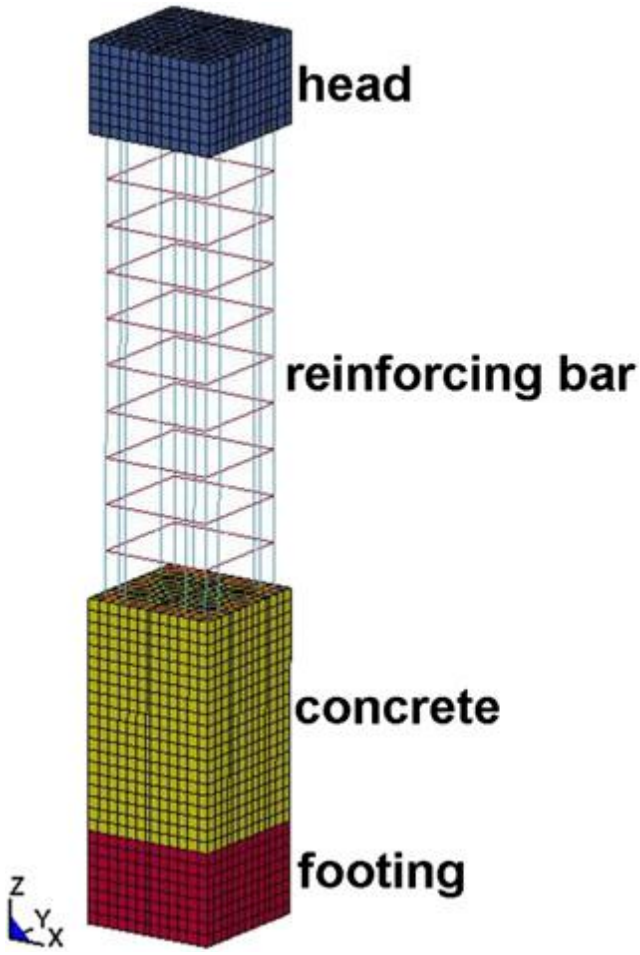

Fig. 1

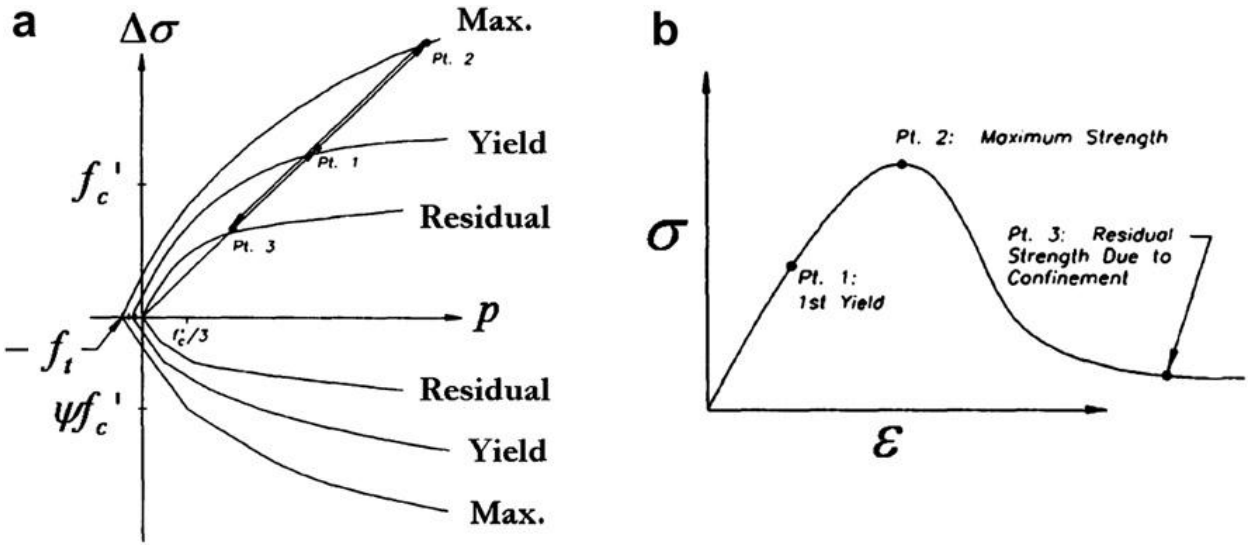
a
Δσ
Max.
Pt. 2
Yield
Pt. 1
Residual
Pt. 3
p
Residual
Yield
Max.
b
Pt. 2: Maximum Strength
σ
Pt. 3: Residual Strength Due to Confinement
Pt. 1: 1st Yield
ε

Fig. 2

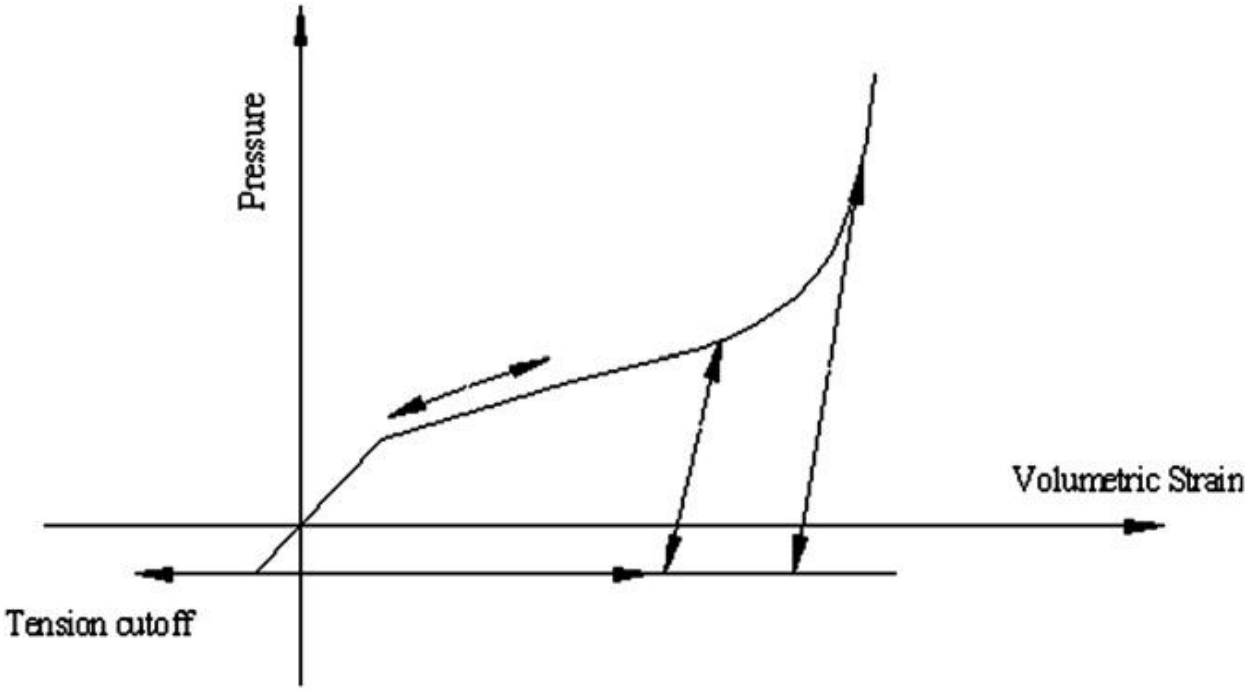

Fig. 3

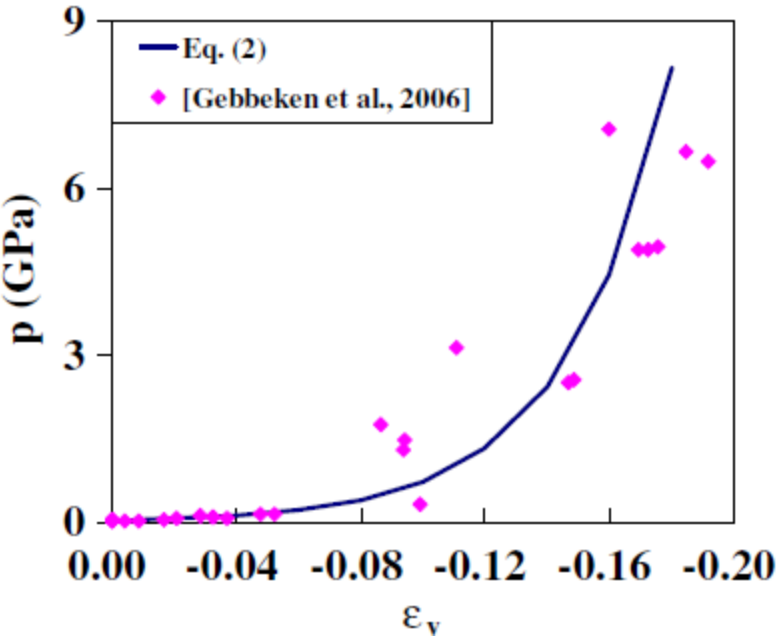
Eq. (2)
[Gebbeken et al., 2006]
p (GPa)
9
6
3
0
0.00
-0.04
-0.08
-0.12
-0.16
-0.20
ε_v

Fig. 4

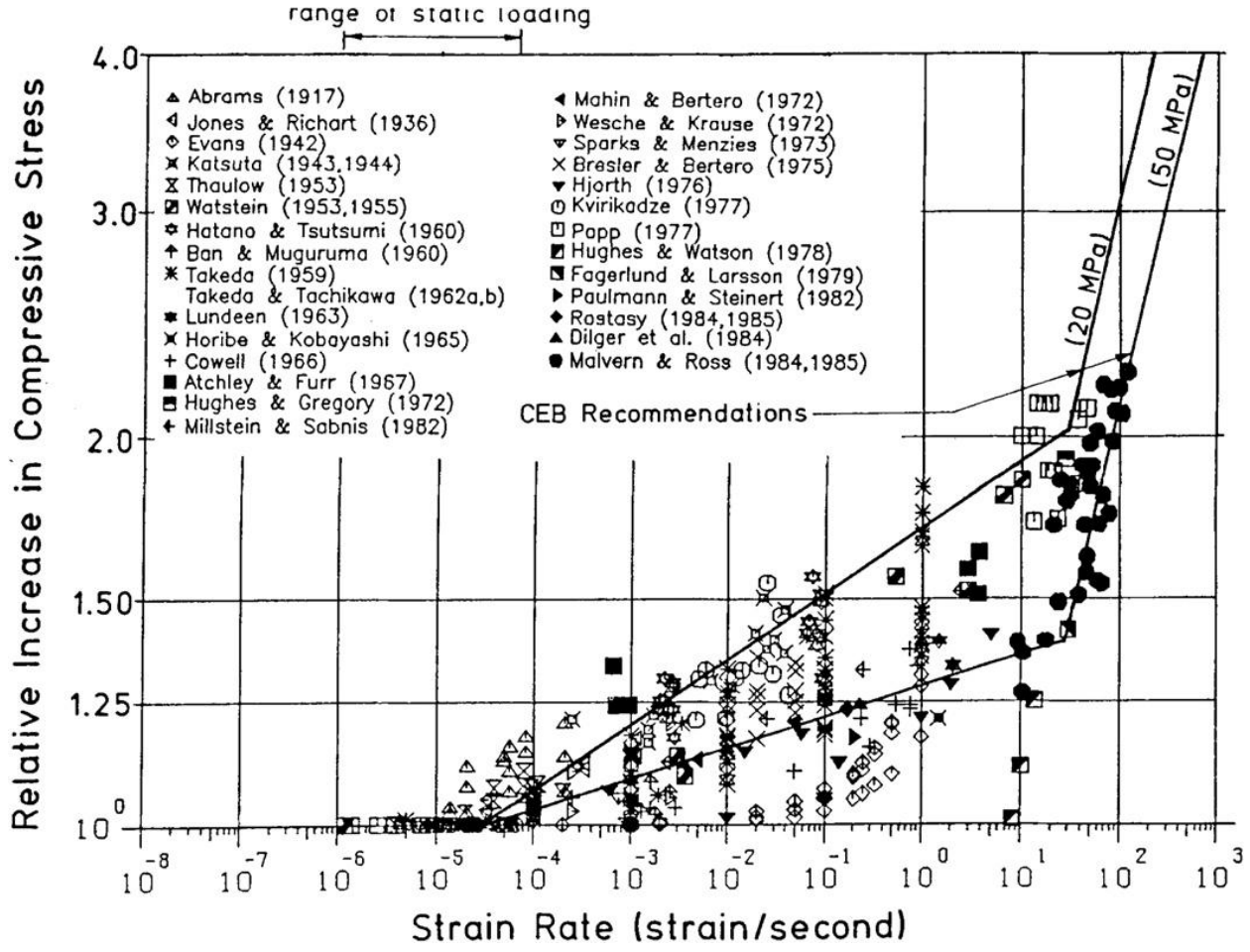
range of static loading
Relative Increase in Compressive Stress
Strain Rate (strain/second)
4.0
3.0
2.0
1.50
1.25
1
Abrams (1917)
Jones & Richart (1936)
Evans (1942)
Katsuta (1943,1944)
Thaulow (1953)
Watstein (1953,1955)
Hatano & Tsutsumi (1960)
Ban & Muguruma (1960)
Takeda (1959)
Takeda & Tachikawa (1962a,b)
Lundeen (1963)
Horibe & Kobayashi (1965)
Cowell (1966)
Atchley & Furr (1967)
Hughes & Gregory (1972)
Millstein & Sabnis (1982)
Mahin & Bertero (1972)
Wesche & Krause (1972)
Sparks & Menzies (1973)
Bresler & Bertero (1975)
Hjorth (1976)
Kvirikadze (1977)
Popp (1977)
Hughes & Watson (1978)
Fagerlund & Larsson (1979)
Paulmann & Steinert (1982)
Rostasy (1984,1985)
Dilger et al. (1984)
Malvern & Ross (1984,1985)
CEB Recommendations
(20 MPa)
(50 MPa)

Fig. 5

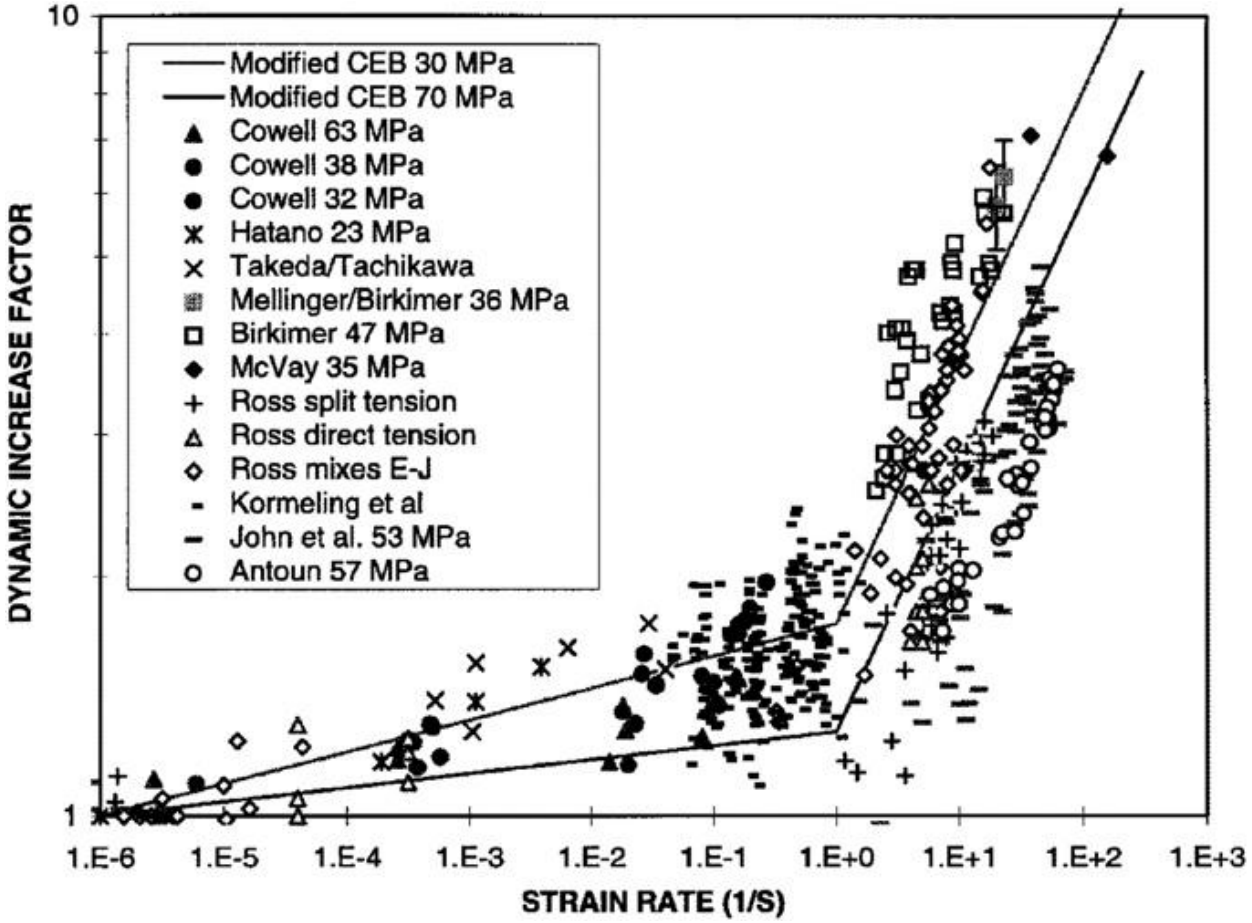
Modified CEB 30 MPa
Modified CEB 70 MPa
Cowell 63 MPa
Cowell 38 MPa
Cowell 32 MPa
Hatano 23 MPa
Takeda/Tachikawa
Mellinger/Birkimer 36 MPa
Birkimer 47 MPa
McVay 35 MPa
Ross split tension
Ross direct tension
Ross mixes E-J
Kormeling et al
John et al. 53 MPa
Antoun 57 MPa
DYNAMIC INCREASE FACTOR
10
1
1.E-6
1.E-5
1.E-4
1.E-3
1.E-2
1.E-1
1.E+0
1.E+1
1.E+2
1.E+3
STRAIN RATE (1/S)
Fig. 6

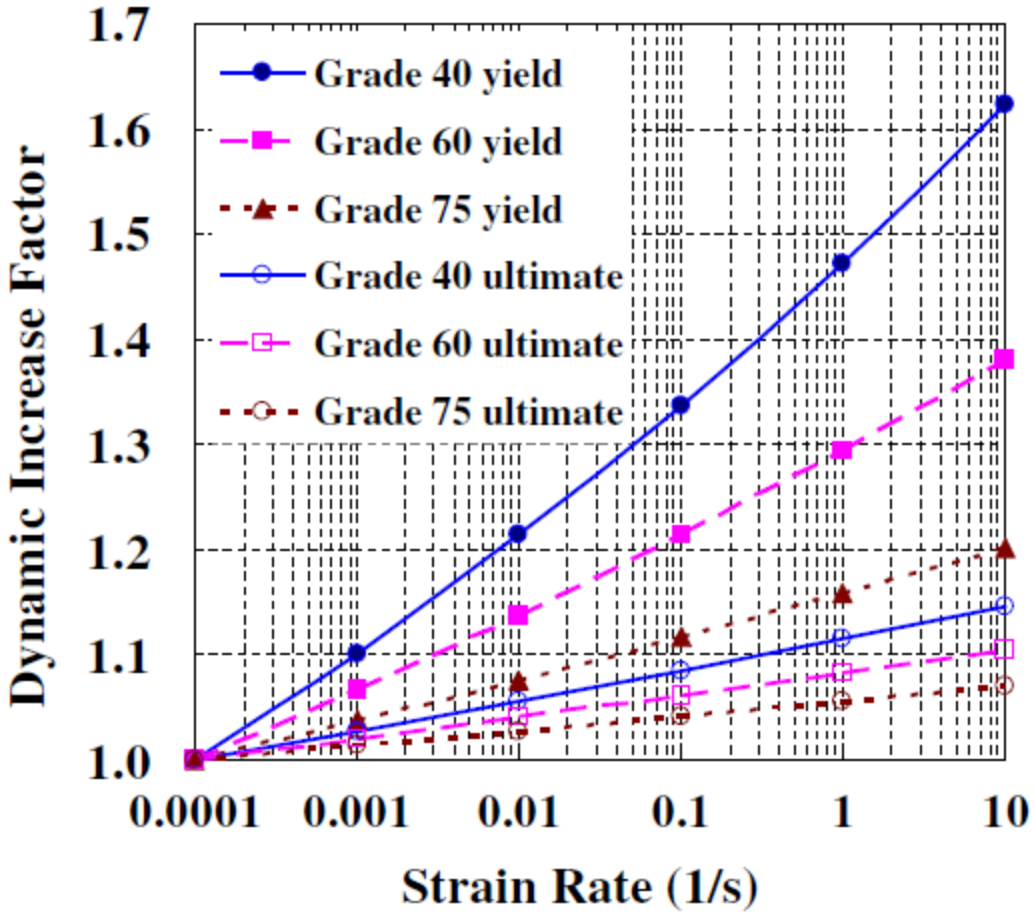
Dynamic Increase Factor
1.7
1.6
1.5
1.4
1.3
1.2
1.1
1.0
Grade 40 yield
Grade 60 yield
Grade 75 yield
Grade 40 ultimate
Grade 60 ultimate
Grade 75 ultimate
0.0001
0.001
0.01
0.1
1
10
Strain Rate (1/s)

Fig. 7

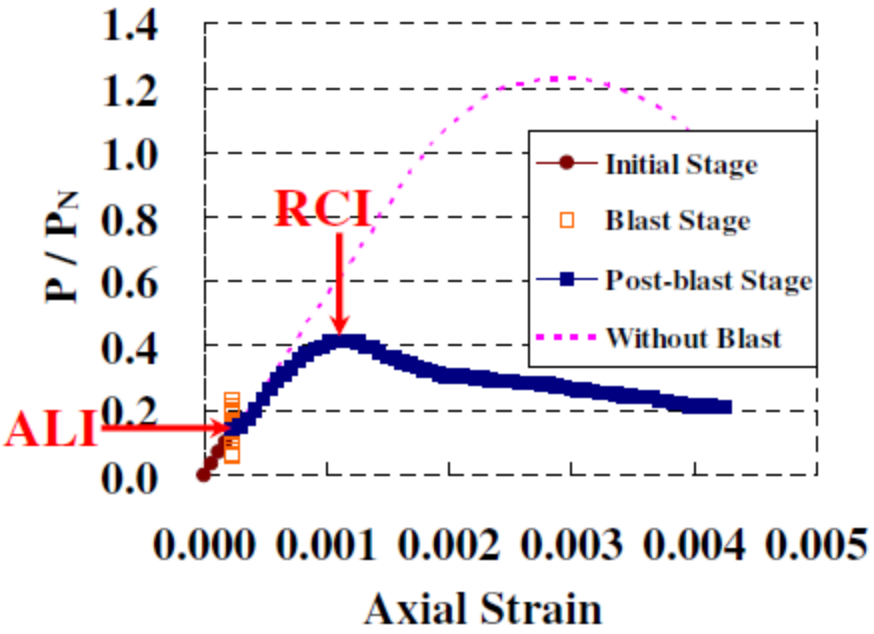
1.4
1.2
1.0
0.8
0.6
0.4
0.2
0.0
P / P_N
RCI
ALI
Initial Stage
Blast Stage
Post-blast Stage
Without Blast
0.000 0.001 0.002 0.003 0.004 0.005
Axial Strain

Fig. 8

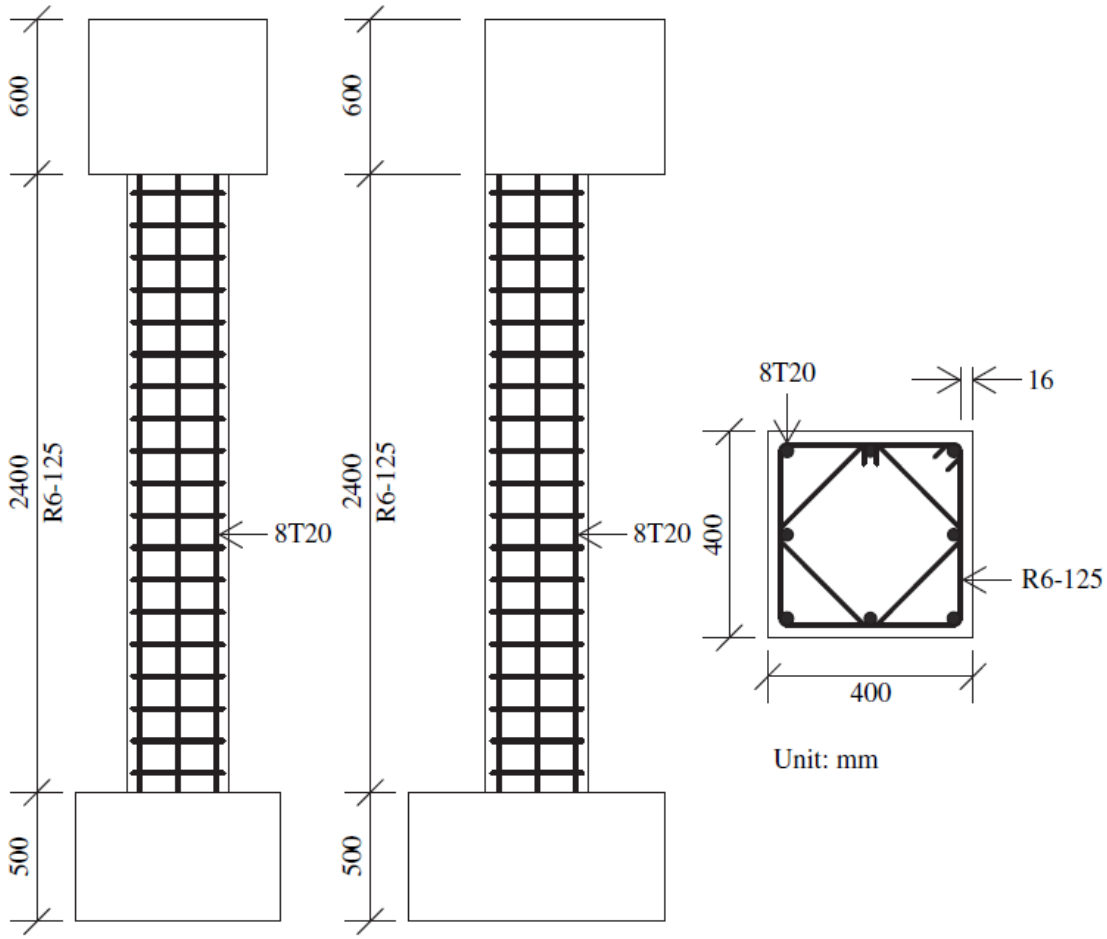
600
2400
R6-125
8T20
500
600
2400
R6-125
8T20
500
8T20
16
400
R6-125
400
Unit: mm

Fig. 9

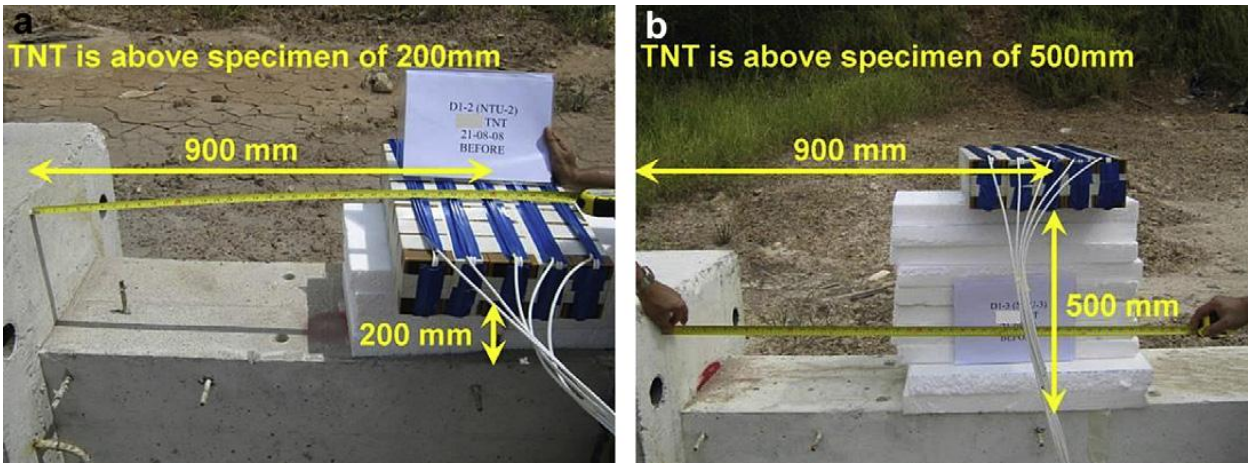
a
TNT is above specimen of 200mm
900 mm
200 mm
b
TNT is above specimen of 500mm
900 mm
500 mm
Fig. 10

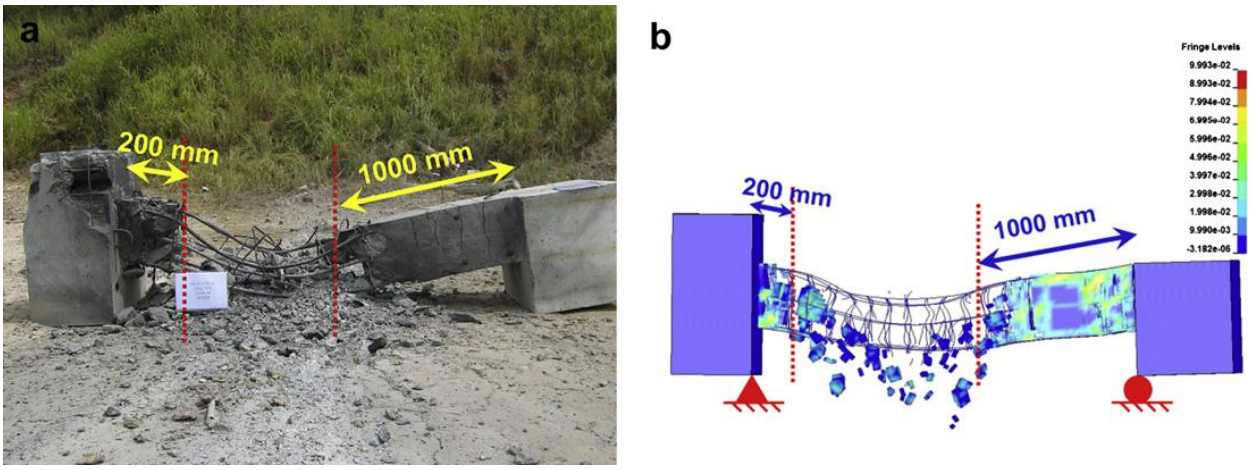
a
200 mm
1000 mm
b
Fringe Levels
9.993e-02
8.993e-02
7.994e-02
6.995e-02
5.996e-02
4.996e-02
3.997e-02
2.998e-02
1.998e-02
9.990e-03
-3.182e-06
200 mm
1000 mm

Fig. 11

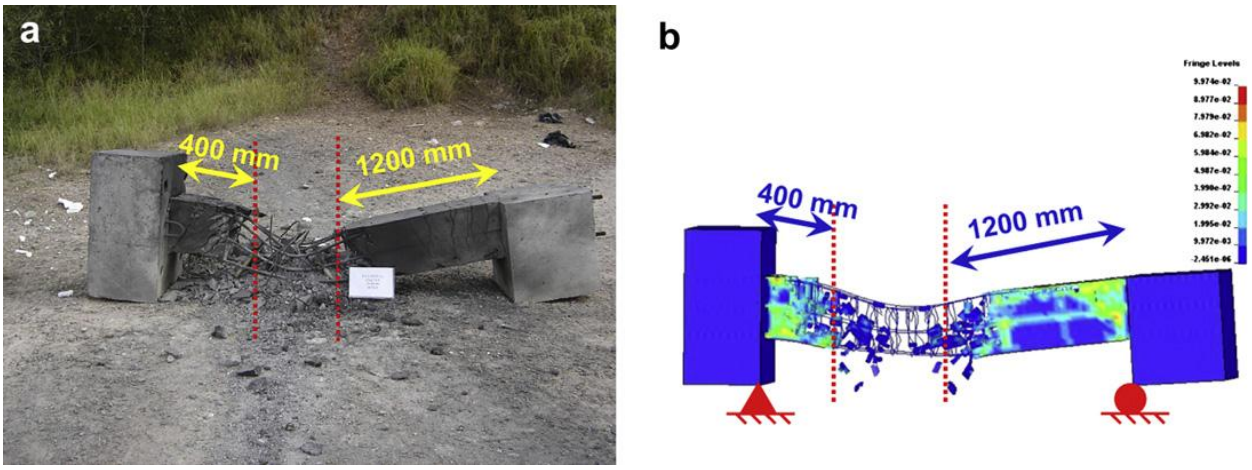
a
400 mm
1200 mm
b
Fringe Levels
9.974e-02
8.977e-02
7.979e-02
6.982e-02
5.984e-02
4.987e-02
3.990e-02
2.992e-02
1.995e-02
9.972e-03
-2.461e-06
400 mm
1200 mm

Fig. 12

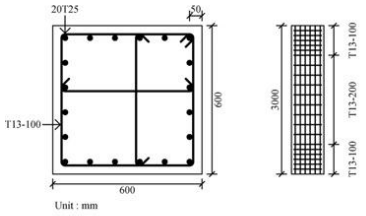

RC61

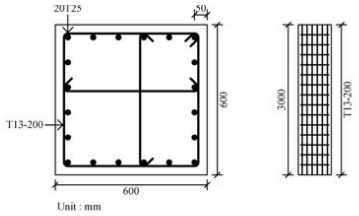

RC62

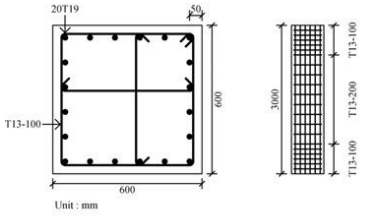

RC63

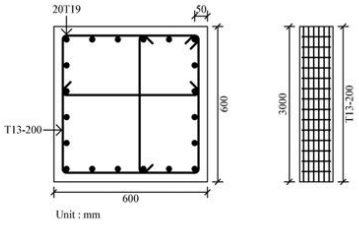

RC64

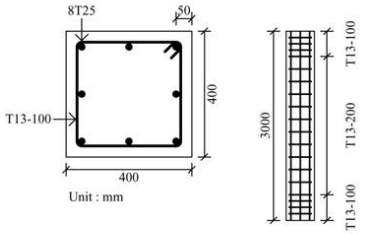

RC41

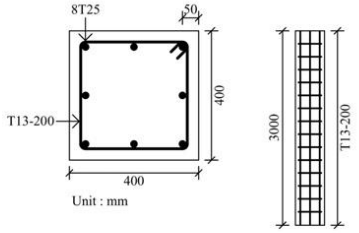

RC42

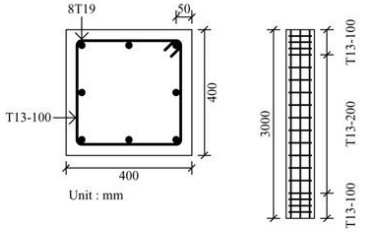

RC43

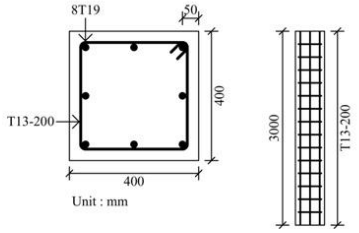

RC44

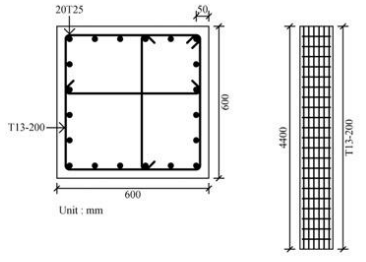

RC621

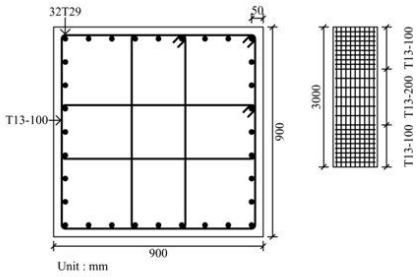

RC9

Fig. 13

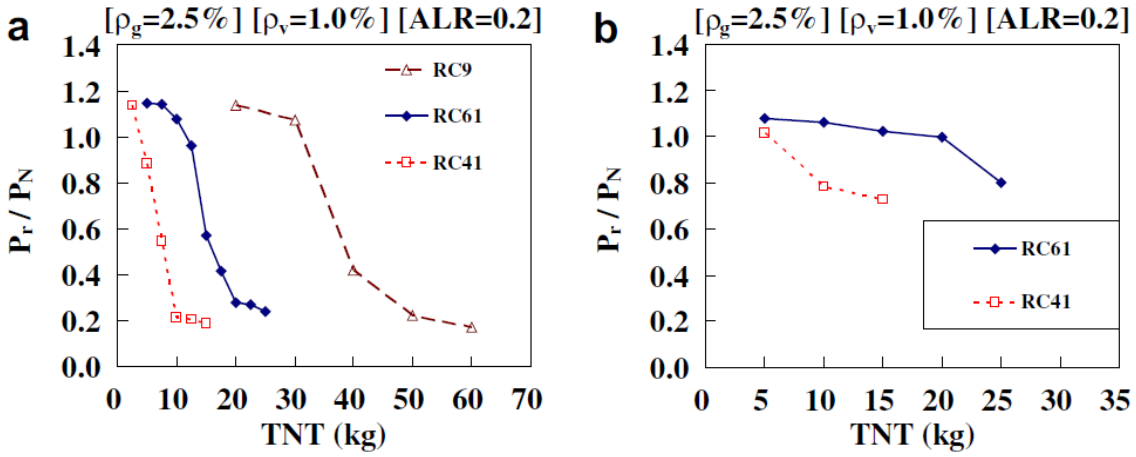
a
[ρg=2.5%] [ρv=1.0%] [ALR=0.2]
Pr / PN
TNT (kg)
RC9
RC61
RC41
b
[ρg=2.5%] [ρv=1.0%] [ALR=0.2]
Pr / PN
TNT (kg)
RC61
RC41

Fig. 14

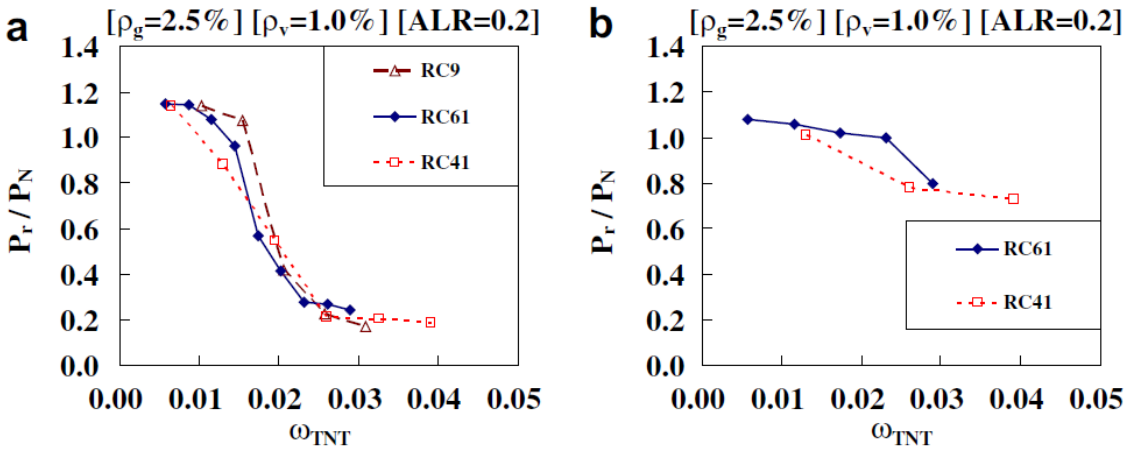
a
[ρg=2.5%] [ρv=1.0%] [ALR=0.2]
Pr / PN
ωTNT
RC9
RC61
RC41
b
[ρg=2.5%] [ρv=1.0%] [ALR=0.2]
Pr / PN
ωTNT
RC61
RC41

Fig. 15

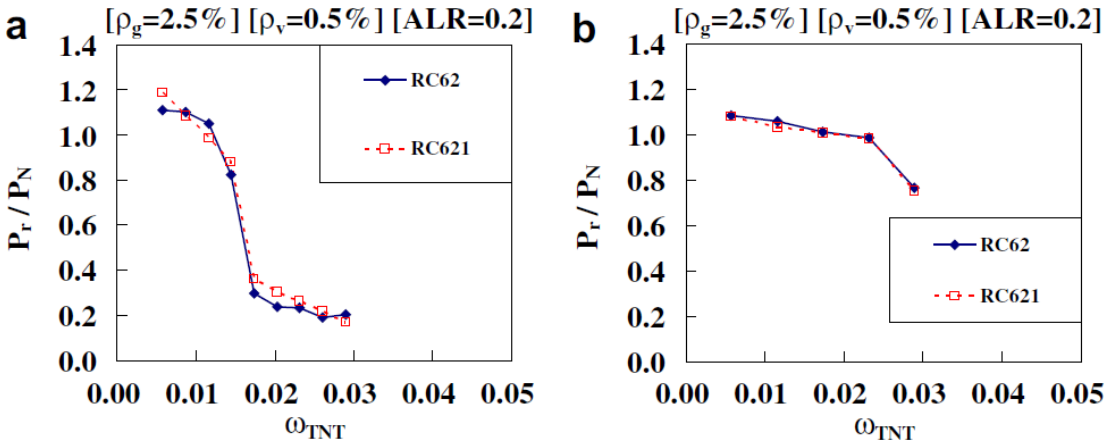
a
[ρg=2.5%] [ρv=0.5%] [ALR=0.2]
Pr / PN
ωTNT
RC62
RC621
b
[ρg=2.5%] [ρv=0.5%] [ALR=0.2]
Pr / PN
ωTNT
RC62
RC621

Fig. 16

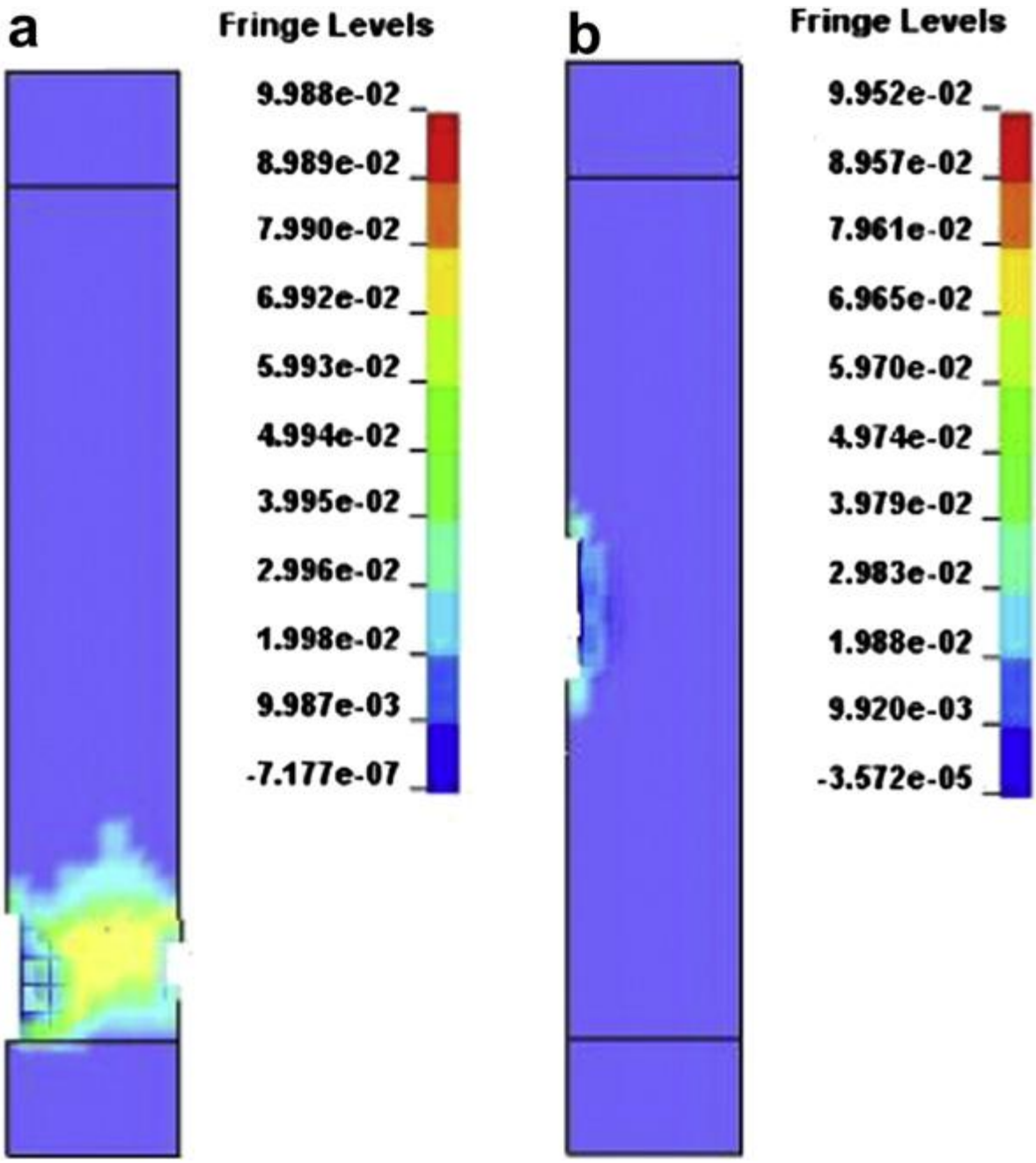
a
Fringe Levels
9.988e-02
8.989e-02
7.990e-02
6.992e-02
5.993e-02
4.994e-02
3.995e-02
2.996e-02
1.998e-02
9.987e-03
-7.177e-07
b
Fringe Levels
9.952e-02
8.957e-02
7.961e-02
6.965e-02
5.970e-02
4.974e-02
3.979e-02
2.983e-02
1.988e-02
9.920e-03
-3.572e-05

Fig. 17

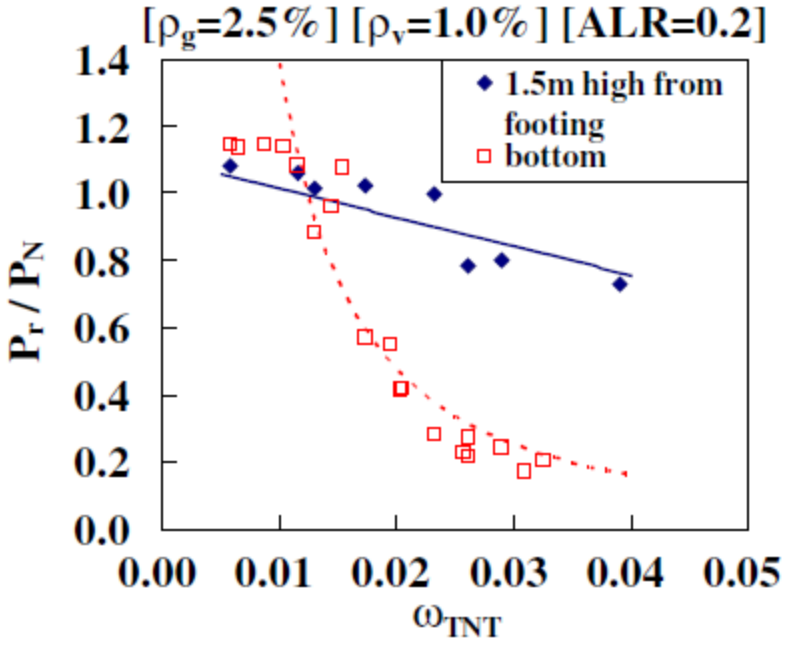
[ρg=2.5%] [ρv=1.0%] [ALR=0.2]
1.5m high from footing
bottom
Pr / PN
ωTNT
1.4
1.2
1.0
0.8
0.6
0.4
0.2
0.0
0.00
0.01
0.02
0.03
0.04
0.05

Fig. 18

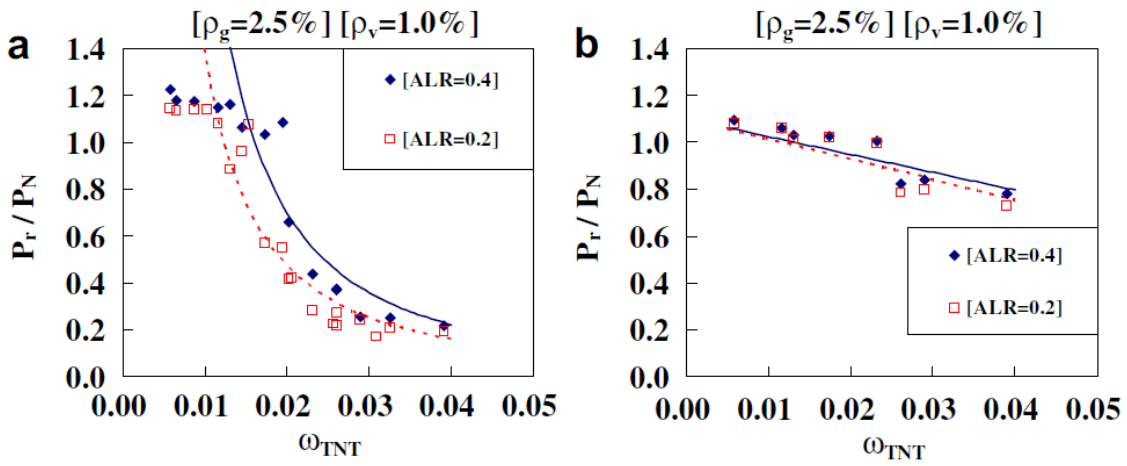
a
[ρg=2.5%] [ρv=1.0%]
[ALR=0.4]
[ALR=0.2]
Pr / PN
ωTNT
b
[ρg=2.5%] [ρv=1.0%]
[ALR=0.4]
[ALR=0.2]
Pr / PN
ωTNT

Fig. 19

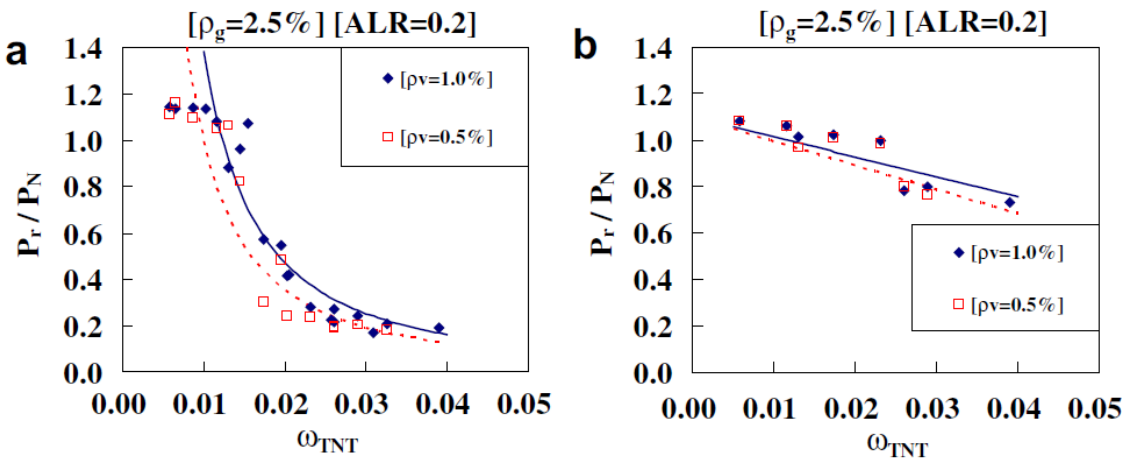
a
[ρg=2.5%] [ALR=0.2]
Pr / PN
ωTNT
[ρv=1.0%]
[ρv=0.5%]
b
[ρg=2.5%] [ALR=0.2]
Pr / PN
ωTNT
[ρv=1.0%]
[ρv=0.5%]

Fig. 20

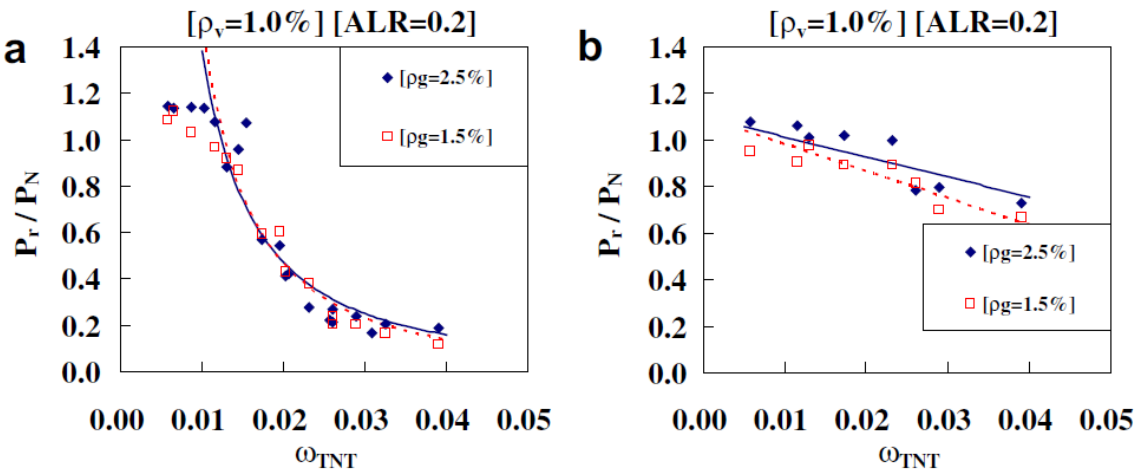
a
[ρv=1.0%] [ALR=0.2]
[ρg=2.5%]
[ρg=1.5%]
Pr / PN
ωTNT
b
[ρv=1.0%] [ALR=0.2]
[ρg=2.5%]
[ρg=1.5%]
Pr / PN
ωTNT

Fig. 21

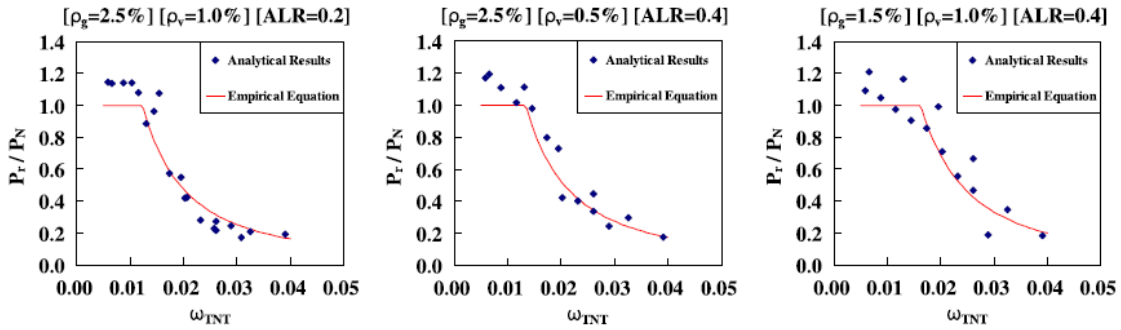
[ρg=2.5%] [ρv=1.0%] [ALR=0.2]
[ρg=2.5%] [ρv=0.5%] [ALR=0.4]
[ρg=1.5%] [ρv=1.0%] [ALR=0.4]
Analytical Results
Empirical Equation
Pr / PN
ωINT

a

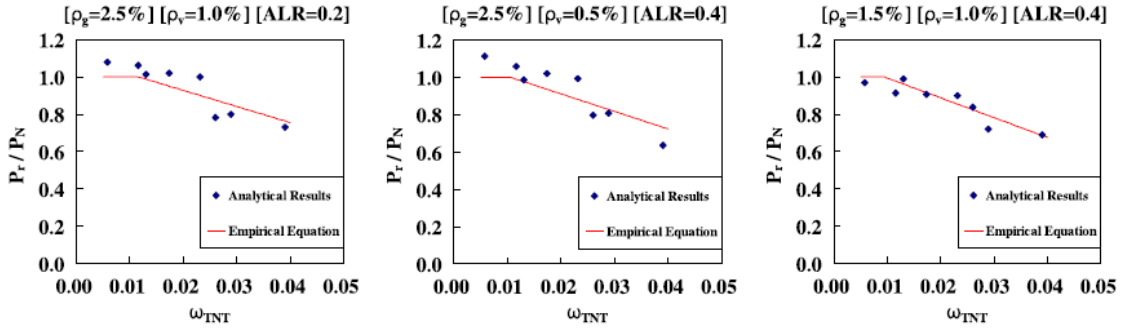
[ρg=2.5%] [ρv=1.0%] [ALR=0.2]
[ρg=2.5%] [ρv=0.5%] [ALR=0.4]
[ρg=1.5%] [ρv=1.0%] [ALR=0.4]
Analytical Results
Empirical Equation
Pr / PN
ωINT

b

Fig. 22